Applied Physics A (2022) 128: 797
https://doi.org/10.1007/s00339-022-05938-7

**Applied Physics A**
**Materials Science & Processing**


# Formation of gold/silver composite nanoparticles by pulsed laser ablation of gold–silver layered films in liquid

**Zsolt Homik[1] · Judit Kopniczky[1] · Tamás Smausz[1] · Dániel Berkesi[2] · Béla Hopp[1,3]**

Received: 20 May 2022 / Accepted: 5 August 2022 / Published online: 20 August 2022


**Abstract**
Nanoparticles of high purity can be produced from a variety of materials by pulsed laser ablation of solids in liquid. Composite nanoparticles are of great importance in various applications such as catalysis or biomedicine and the process of their formation is still a subject of intense research. In this work, gold/silver composite nanoparticles were synthesized in aqueous media by ns pulsed laser ablation of gold–silver multilayer targets with different absolute layer thicknesses and layer thickness ratios. The generated nanoparticles showed a log-normal distribution of sizes, with average diameter in the 20–40 nm range and standard deviation of 9–30 nm. By comparing the UV–VIS absorbance spectra of the nanoparticle colloids with two theoretical calculations (based on the Mie and the BEM model), it was found that there is a direct correlation between the average Au and Ag content of the nanoparticles and the composition of the films on the substrate. Assuming thermal ablation, our model calculations showed that there is a maximum thickness of the top layer up to which both layers can be ablated simultaneously and alloy nanoparticles can be produced.

## 1 Introduction

Over the past decades, the versatility and unique chemical, electrical, magnetic, and optical properties of nanoparticles (NPs) with different compositions have led to their rapidly growing range of applications. They are used, for example in drug delivery [1, 2], bioimaging [3], cancer diagnosis and therapy [4, 5], solar cells and collectors [6, 7], electrochemical energy storage [8] and generation [9, 10], biosensors [11, 12], chemical sensors [13, 14], and surface-enhanced Raman-spectroscopy (SERS) [15–17]. The diversity of applications and needs continues to encourage research to develop new nanoparticle production methods.

There is a particular interest in multi-element NPs with unique and controllable properties. Alloy nanoparticles offer the possibility to tune functional properties (e.g., local surface plasmon resonance and/or adsorption energies) for sensing or catalytic applications [18, 19].There are three basic ways to synthesize alloy NPs [20]. Chemical methods use (electro)chemical reduction [21, 22], chemical precipitation [23], hydrothermal synthesis [23, 24], etc. in the production process. The main drawbacks of chemical methods are the presence of impurities, the use of hazardous chemicals [25, 26] and the complexity of the synthetic processes [27, 28]. NPs can also be produced using a biological approach. Microorganisms-like bacteria, yeasts, fungi, and viruses [29], or plants [30] or even agricultural and industrial waste [31] can be the source of alloy NPs. However, the complexity of the parameters and constituents usually pose limitations when it comes to controlling the size and shape of NPs [29, 32]. Another option is using traditional physical processes such as mechanical milling [33], sputtering [34], spark discharge [15, 35], and electro-explosion [36]. These methods generally have the disadvantage of low efficiency, high energy needs or the presence of impurities.

For the synthesis of colloidal NPs, pulsed laser ablation in liquid, i.e., the PLAL technique offers the advantages of a single experimental setup, low costs, the purity of the colloid product, being an environmentally friendly procedure and the controllability of the NPs' parameters [37–39]. The key advantage of PLAL for the synthesis of NPs with innovative

✉ Zsolt Homik
hzsolt1996@gmail.com

[1] Department of Optics and Quantum Electronics, University of Szeged, Dóm tér 9, Szeged 6720, Hungary

[2] Department of Applied & Environmental Chemistry, University of Szeged, Rerrich Béla tér 1, Szeged 6720, Hungary

[3] Department of Materials Science, Interdisciplinary Excellence Centre, University of Szeged, Dugonics tér 13, Szeged 6720, Hungary

composition is the fast kinetics of NP formation [40]. During PLAL, the laser irradiated area heats up to temperatures of 103–104 K, and a plasma plume is generated. Due to the extreme temperature and pressure conditions, the plasma expands into the liquid environment and a cavitation bubble emerges, which contains the target material in the form of droplets and vapour. NP generation takes place in the plasma plume and in the cavitation bubble [40]. After the collapse of the cavitation bubble, a colloid of NPs is obtained. The processes involved in the early stages of PLAL and the effects of target, liquid, and laser conditions on the NPs' properties have been widely studied both experimentally and theoretically [41–44].

To prepare metal alloy NPs bulk alloys or metal powder mixtures are most commonly applied as targets [45, 46]. At the same time, thin metal films either as homogeneous metal alloy films or as segregated metal bilayers/multilayers are less frequently used [47–49], although they might be significant. Nikov et al. successfully produced gold–silver nanoparticles by PLAL of bimetallic thin films [50], and established a linear dependence of the surface plasmon resonance (SPR) maximum of the colloidal NPs on the metal concentration of the films. They studied the influence of the laser parameters and film thickness on the morphology, particle-size distribution, and optical properties of the obtained colloidal NPs [51].

Amendola et al. and Lin et al. demonstrated that the use of multilayer films as target material in the ablation process is suitable for the fabrication of alloy NPs [52, 53]. The combination of pure metal layers in the substrate and the choice of liquid medium allowed to control the chemical processes, which is of great importance in the synthesis of multi-element NPs. The results of a joint computational and experimental study of the nanoparticle formation in ultrashort PLAL of Ag–Cu bilayer films, presented by Cheng-Yu Shih et al., provided clear evidence of a limited mixing between the two components of the bilayer films [54].

Thus, since PLAL is a promising technique for the production of designed NPs using thin film targets, we aimed to study the process in more detail. We applied a set of Au/Ag bilayer film combinations as targets and investigated the ablated NPs optical properties, size distributions and compositions. We compared the experimental results with theoretical models and tried to give an interpretation of the ablation process on the basis of a simple temperature model.

## 2 Experimental methods

### 2.1 Synthesis

Cr/Ag/Au multilayers were prepared on fused silica substrates. The substrates were cleaned with acetone/methanol mixture and Ar-plasma cleaning was used to remove any surface contaminants before deposition. To increase adhesion between the silica substrate and the silver layer, a 2 nm thick chromium bonding layer was first deposited by electron beam evaporation. Silver and gold layers were deposited by thermal evaporation using wolfram boats. Each deposition process was performed at a working pressure of 3E-5 mbar, and the layer thickness was controlled by quartz crystal microbalance. The deposition rates were 0.1 nm/sec for Cr, 0.5 nm/sec for Ag and 1 nm/sec for Au. Since only one thermal evaporation source (one boat) could be used at a time in the coating chamber, a venting & evacuating cycle had to be inserted between the deposition of the silver and gold layers. To avoid oxidization, gold films were always on top of silver films (except in the reference samples). For PLAL substrates, seven different gold/silver layer combinations were prepared (fixed 50 nm gold layer on 20, 50 and 200 nm silver layers; and 20, 50, 100, and 200 nm gold layers on fixed 100 nm silver layer, respectively). For reference, pure silver and gold layers of 50 and 200 nm thickness were used.

For the PLAL process a pulsed Nd-YAG laser (Quantel, operated at wavelengths of 1064 nm and 532 nm, a pulse duration of 8 ns and a repetition rate of 6.67 Hz) was applied. The laser energy was 4.25 mJ for both wavelengths, and the pulses were focused by a lens (focal length f = 5 cm) to a 300 µm diameter beam spot, resulting in a fluence of 6.01 J/cm$^2$. Fig. 1 shows the schematic of the experimental setup. The 2 × 2 cm$^2$ target was immersed in 3 ml distilled water. The laser beam passed through the approx. 7 mm thick water column and was focused on the target surface. The substrate holder was mounted on a programmable, motorized x–y translating stage, which made it possible to ablate the target in an automated scanning process. To ensure that by each shot a different spot of the target is ablated, the speed of the stage translation was set to 2 m/s. Nanoparticle colloidal solutions were obtained after ~ 20 min (8,000 pulses) of ablation.

### 2.2 Characterization

We studied the morphology and size distribution of the NPs using Scanning Electron Microscopy (SEM, Hitachi S-4700 FESEM) and Transmission Electron Microscopy (TEM, FEI Tecnai G2 20 X-TWIN). Prior to imaging, small amounts of the colloidal solutions were dropped and allowed to dry on the surface of a clean Si-plate and highly oriented pyrolytic graphite (HOPG). We investigated 300 to 1300 particles/sample with the help of ImageJ software. To determine the elemental composition of the NPs, Energy Dispersive X-ray spectroscopy (SEM–EDX, RÖNTEC XFlash Detector) analysis was performed. The UV–VIS absorbance spectra of the colloidal solutions were recorded using a UV-2101PC scanning spectrophotometer. The absorbance spectrum of the

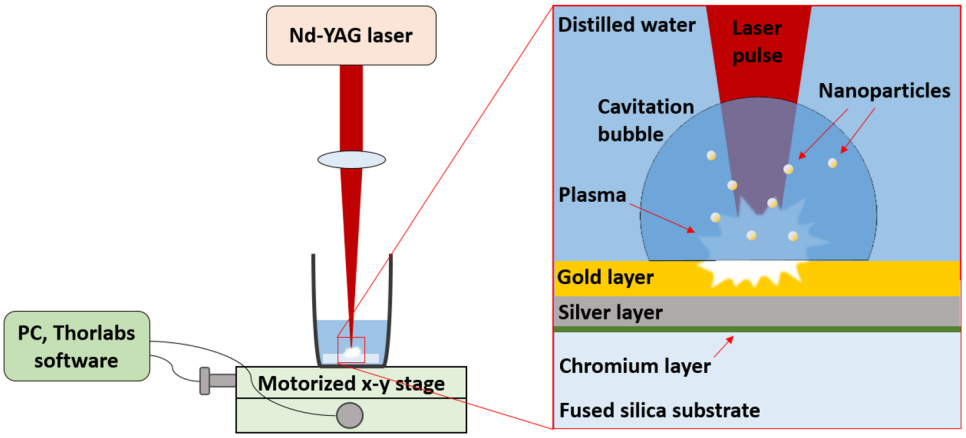


**Fig. 1** Schematic of the experimental setup

reference distilled water was subtracted in real time. The optical properties of the NPs were modelled and compared to the experimental data. For modelling, a Mie model and a boundary element method (BEM)-based simulation were performed using the Mieplot 4.6.19 software [55] and the MNPBEM® Mathlab toolbox [56]. The optical constants necessary for the simulations were taken from [57], and the average particle size and size distribution data were obtained from the SEM analysis. We developed a thermal model using the COMSOL software. The physical properties of the materials were taken from COMSOL's built-in libraries and [58, 59].

## 3 Results and discussion

Typical SEM and TEM images of the NPs generated by PLAL of the layered substrates are shown in Fig. 2. Regarding the morphology of the NPs seen by SEM, most NPs with gold content are well separated spherical particles. However, the silver NPs are often embedded in an amorphous precipitate, and are barely distinguishable. Probably an oxidation and/or aggregation effect is involved in the case of silver. TEM images show that there are many particles with sizes below the resolution limit of the SEM. Thus, we suspect that NPs ‹10 nm are underrepresented in the size distribution plots based on the analysis of SEM images. Due to the aggregation and/or oxidation effects mentioned above, the size distribution of pure silver NPs cannot be determined. In all other cases, log-normal particle-size distribution can be observed (shown in Fig. 3). These results are in good agreement with the literature [53, 60]. The precise determination of the particle boundaries was often hampered by the aggregation of particles too. We found that the size of NPs depends neither on the absolute thickness of the layers nor on the ratio of layer thicknesses. The fitted log-normal curves show that the mean value of the particle sizes is in the 20–40 nm range, with a standard deviation of 9–30 nm.

Comparing NPs generated with 532 nm and 1064 nm laser pulses, no significant differences in morphology and size distribution were observed. However, ablation with 1064 nm laser pulses resulted in a higher nanoparticle yield.

The SEM–EDX measurements (Fig. 4) indicate that most of the material surrounding the NPs is also an ablation product, but consists either of very small particles (i.e., their size falls below the resolution limit of SEM) or of some Ag/Au containing precipitate. It must be noted that the SEM–EDX setup is more appropriate for the qualitative analysis of the composition of NPs than for quantitative analysis.

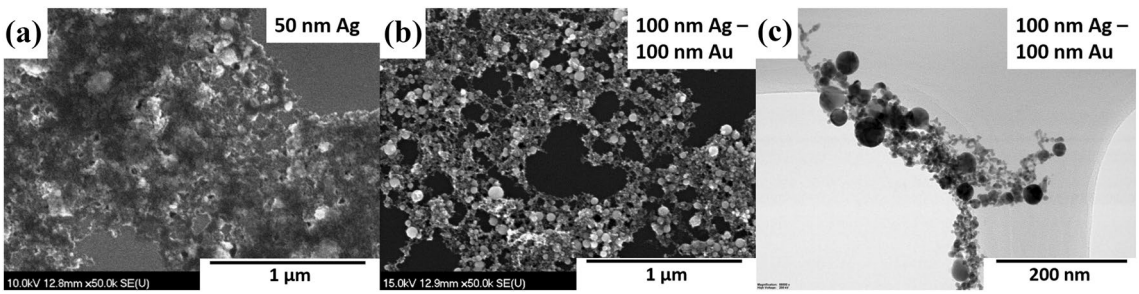


**Fig. 2** Typical SEM (**a**, **b**) and TEM (**c**) images of the PLAL-generated NPs. (The thickness of the silver and silver/gold layer on the substrate is indicated in the upper right corner of the pictures.)

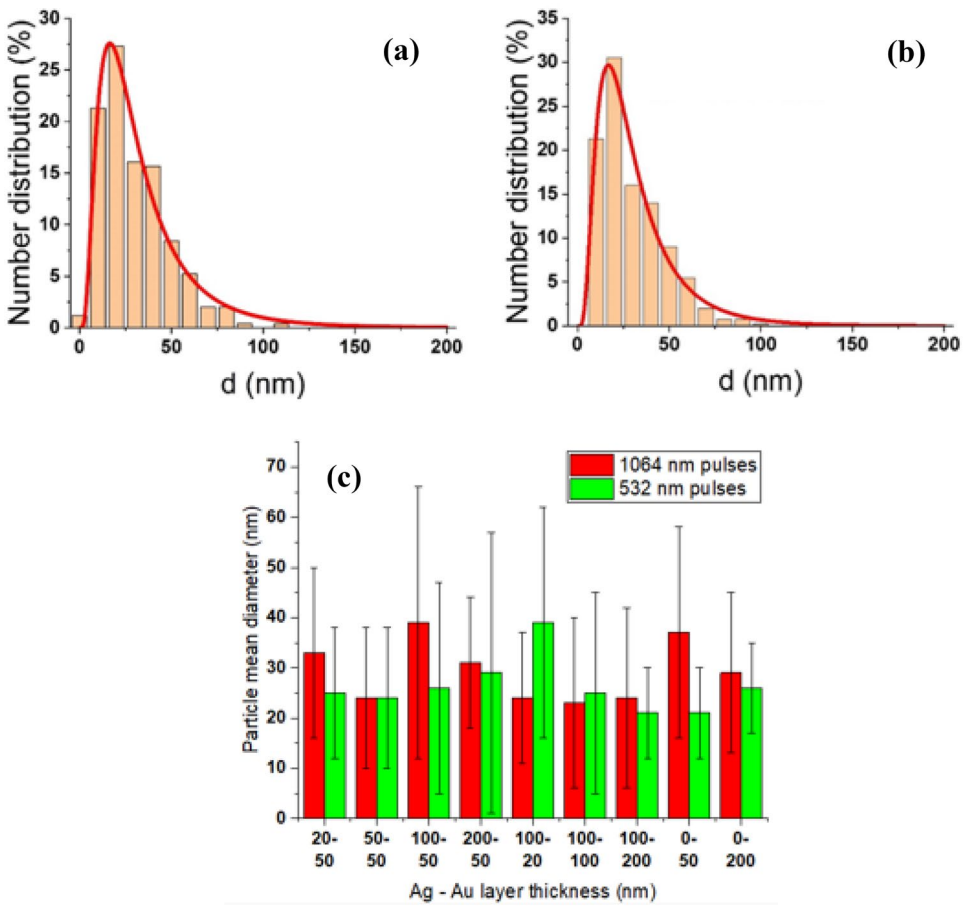


**Fig. 3** Typical size histograms (for 100 nm Ag–100 nm Au in this particular case) of the NPs produced at **a** $\lambda = 532$ nm and **b** $\lambda = 1064$ nm laser wavelengths, and the mean particle diameters (**c**)

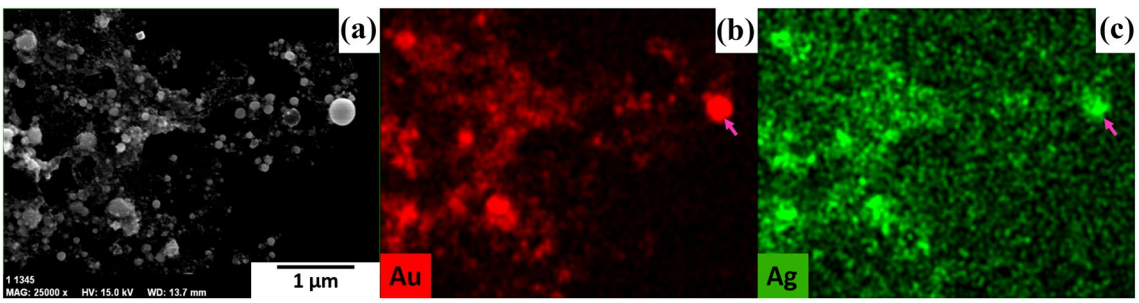


**Fig. 4** SEM–EDX elemental mapping of NPs produced by ablation ($\lambda = 1064$ nm) of the 20 nm Ag + 50 nm Au layered substrate

The element mapping images provide unambiguous evidence that ablation of the multilayer target results in alloy NPs (Fig. 4). However, the images also show that not all of the particles produced are alloyed; some are pure gold or silver. No core–shell structure could be observed. Alloying is not necessarily homogeneous, and domain formation is more probable in the particles (see marked particle in Fig. 4). We note that due to the resolution and detection limit of SEM–EDX, alloying could only be analysed for the larger (> 50–100 nm) particles. Although TEM-XRD measurements could be used to investigate the domains within individual NPs, since the lattice constants of gold and silver are essentially identical, this method is not applicable to Au–Ag alloys.

SEM–EDX line scans (Fig. 5) confirm the alloying for certain layer thickness combinations. The line-scan spectrum shown in Fig. 5a suggests that a 200 nm Au upper layer is too thick for alloying to occur to any significant extent. It also revealed that the composition of the particles varies. It is known that silver has an SPR peak in the absorption spectrum around 400 nm and gold around 530 nm [37] (assuming several 10 nm diameter spherical NPs). It is also known that

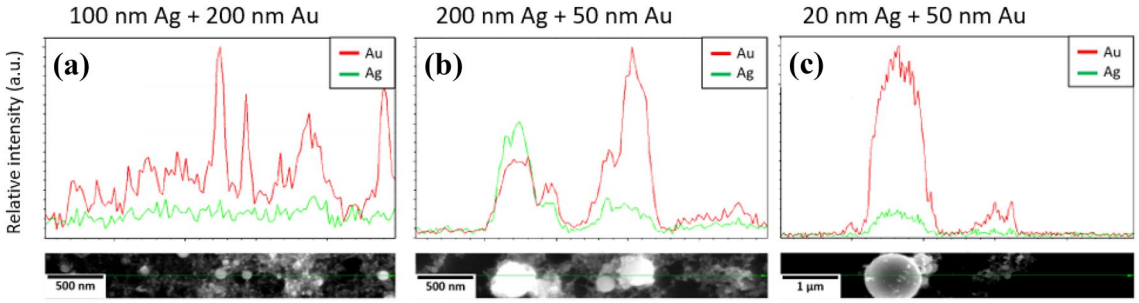


**Fig. 5** EDX elemental line-scan profiles with corresponding SEM images of NPs produced by PLAL of various silver/gold layered substrates (layer thicknesses are indicated above the plots)

for alloy NPs, the SPR peak falls between the SPR peaks of the pure materials and is shifted linearly as a function of the composition ratio [15, 61]. (If the colloidal solution contained a mixture of pure gold and pure silver NPs, the measured absorption spectrum would show two distinct peaks.) Therefore, we recorded the UV–VIS absorbance spectra of the colloidal solutions of the NPs and investigated the shift of the SPR peak as a function of Au–Ag layer thickness combinations on the substrate. In fact, absorbance spectra are related to the average composition of the NP population in the solution.

It is clearly seen in the series of the normalized absorbance spectra of the colloids that the position of the SPR peak is shifted as a function of the Au:Ag layer thickness ratio. This indicates that there is direct correlation between the Au and Ag content of NPs and the composition of the films on the substrate. Since we were primarily interested in the composition of alloy NPs in the colloid, we performed simulations to see where the absorption peaks are for NPs with known Au:Ag composition. First, a simulation based on the Mie model was used assuming spherical NPs of 30 nm with a standard deviation of 50%. The refractive indices of gold–silver alloys were applied to alloys with a composition varying by 10%, from pure gold to pure silver [57]. We found some phenomena that the Mie model could not explain. For this reason, we performed a simulation based on a different approach, called the Boundary Element Method (BEM) [56], for further investigations. The essence of the BEM method is to solve Maxwell's equations in the dielectric environment of bodies with homogeneous and isotropic dielectric functions, separated by abrupt interfaces. By comparing the experimental and the simulation results, three important observations can be made (Figs. 6 and 7).

First, the higher the gold content of the particles, the greater the similarity between the shape of the measured absorbance curves and the theoretical predictions. At higher silver contents, however, the difference becomes more pronounced and is particularly striking when the experimental curves are compared to simulations based on the BEM method (Fig. 6). The reason for this is that, due to computational capacity constraints, only a few particles could be considered with the BEM method. The difference may also be attributed to the fact that silver is more prone to oxidation, so particles with higher Ag content are probably not as spherical as assumed in the theoretical model. In addition, the relatively low signal-to-noise ratio of the measured spectra leads to a broadening of the SPR peak during normalization.

It is also observed that if we plot the SPR peak positions of colloids as a function of Au content in the ablated film and the theoretical curves (i.e., the SPR peak positions as a function of Au content in the simulated NPs) in the same figure, all the recorded SPR peaks are at longer wavelengths than the calculated ones (Fig. 7). Based on the results of Isnaeni et al. [62], we suspect that this difference is (partially) caused by the aggregation of NPs in the colloids. Using the BEM method, we were able to take the aggregation effect into account and thus achieve a better agreement between the theoretical curves and the experimental results.

Finally, it can also be seen in Fig. 7 that the thicker the gold layer is relative to the silver layer, the greater the above discussed difference (i.e., the experimental data points of the SPR peak positions are above the simulation curve). This phenomenon can be explained by the fact that in all cases the gold layer was on top of the silver layer, and as the thickness of the gold layer increased, the laser pulse had a smaller impact on the silver layer. So, although the film had a non-zero silver content ($d_{silver} > 0$), the silver layer was so deep under the thick gold layer that the laser could barely ablate it, and the NPs produced had a higher gold content than we had expected from the Au:Ag ratio in the film. However, the higher gold content of the NP means that its SPR peak position is closer to 540 nm (the SPR peak of pure gold). The same explains why NPs ablated from the 100 nm Ag–100 nm Au films have a higher gold content than those ablated from the 50 nm Ag–50 nm Au films (even though the Au:Ag ratio is the same in the two films). We also observed that the SPR peak positions of

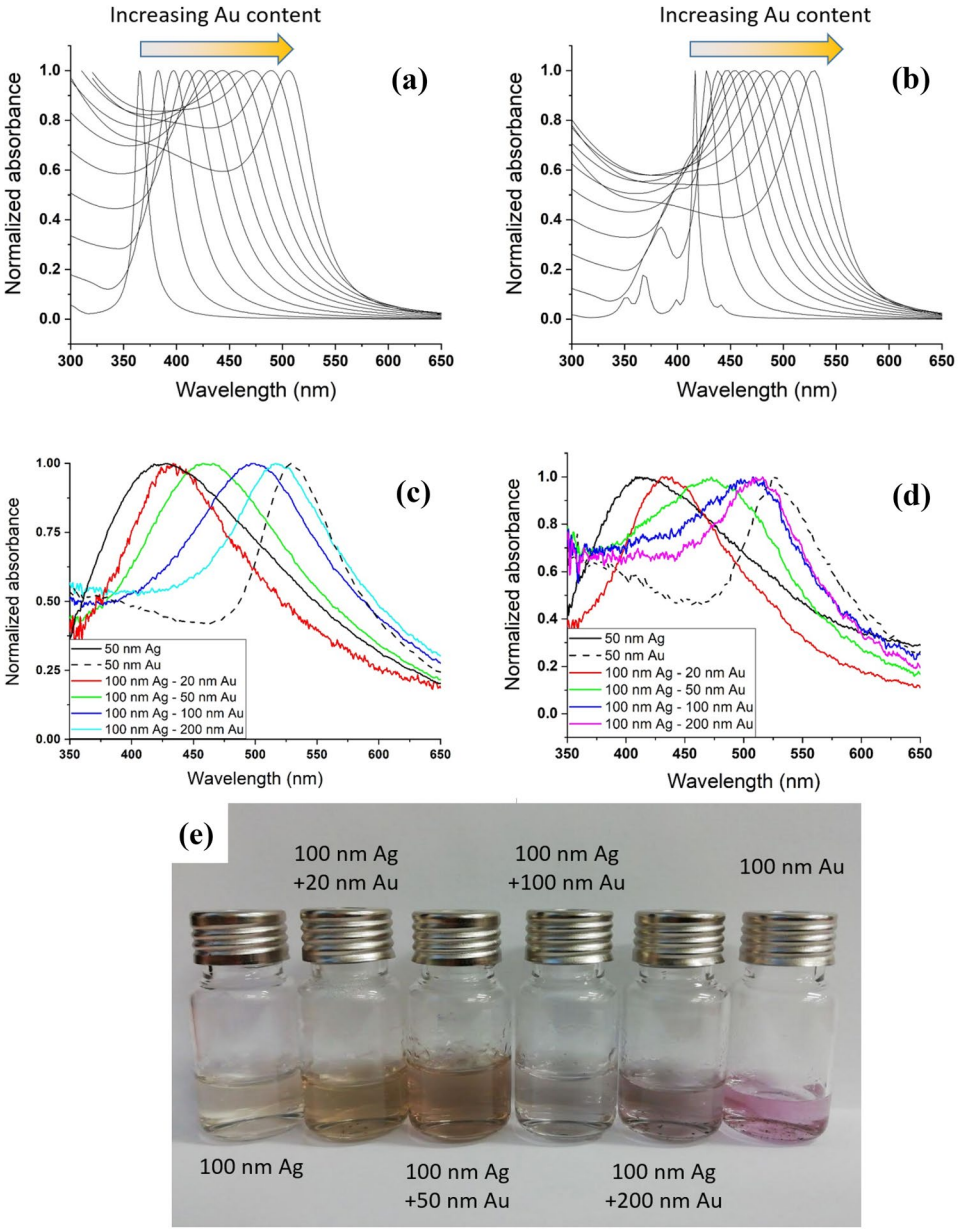


**Fig. 6** Mie (**a**) and BEM solver (**b**) simulated absorbance spectra of alloy NPs with gradually increasing Au content (10% more Au from left to right in the successive curves). Measured absorbance spectra of the colloids for 1064 (**c**) and 532 nm (**d**) laser pulses. **e** shows a picture of colloids made with different layer combinations

NP colloids produced with laser pulses at $\lambda = 1064$ nm are much closer to the simulated values, especially for thinner gold layers. This may be because the photothermal effect of the ablation is more pronounced for 1064 nm pulses than for 532 nm pulses. During thermal ablation, the heat conduction allows the complete and rapid evaporation of the material forming the layers, and so, alloy NPs with a composition ratio that closely approximates the layer thickness ratio can be produced.

When comparing PLAL with 532 and 1064 nm laser pulses, we found that the absolute value of absorbance was significantly higher for 1064 nm pulses (Fig. 8). This is most probably due to the higher nanoparticle yield at the higher laser wavelength.

The morphology and composition of the ablation craters were also investigated by SEM and SEM–EDX (Fig. 9). As can be seen in images a and d, the shape of the ablation craters corresponds to the shape of the Gaussian beam profile. The EDX images show that for thicker gold layers, more silver is detected in the residual crater material. For the 200 nm Au–100 nm Ag sample (a–c), it can be seen that while the gold in the irradiated areas has basically disappeared, the signal from the silver is clearly visible in the same locations. This observation can be explained on the one hand by the fact that some of the silver is re-deposited back to the sample during the ablation process, and on the other hand by the fact that with a thicker gold layer, the deeper silver layer is only partially

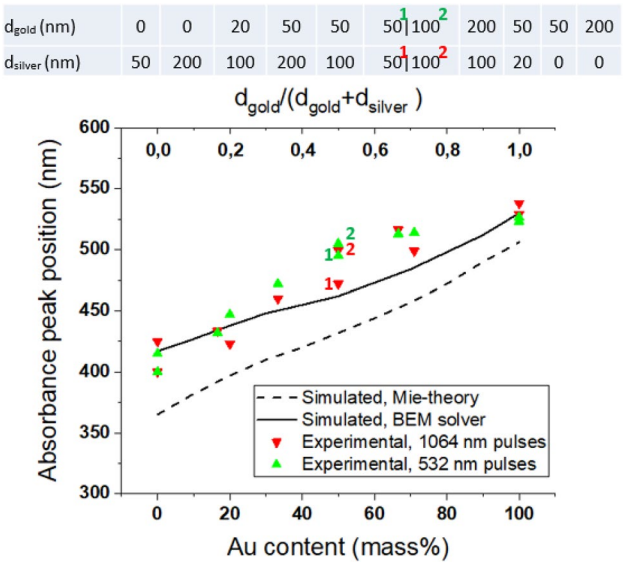


**Fig. 7** Comparison of experimental and simulation results. Note that the experimental results are plotted as a function of Au ratio in the film ($d_{gold}/(d_{gold}+d_{silver})$), while the theoretical curves as the Au content in the NPs. In case of 50% Au in the film, we had measurements with two different absolute layer thicknesses (marked (1, 2) both in the table and the plot)

removed from the sample. This observation supports the result in the case of 200 nm gold layer the silver does not participate in nanoparticle formation. In the case of 50 nm Au–100 nm Ag (d–f), both the gold and the silver layer is fully evaporated at the irradiated sites. It is also observed that the signal from the gold and silver layers suppresses the signal from the deepest chromium layer, so in the irradiated areas, where the top two layers are thinned/fully evaporated, the signal from the chromium layer is apparently enhanced (c, f).

Although it cannot be seen in the absorbance spectra of the NP colloids, the SEM–EDX images of dried droplets of the colloids show that trace amounts of Cr and Si elements are also present (Fig. 10). This suggests that, especially in the case of thin Au–Ag layers, both the Cr bonding layer and the fused silica substrate are ablated during the PLAL process. EDX mappings imply that chromium is mainly represented as separate spherical $CrO_x$ microparticles and it does not form alloys. Silicon also occurs as oxide (most likely in the form of $SiO_2$), but it does not form particles and appears to be more uniformly distributed in the colloid.

## 4 Theoretical study

To study how the different combinations of thin films on the substrate affect the composition of NPs produced during PLAL, an in-depth time-dependent temperature model of the ablation process, similar to that seen in the work of Min Qiu and his colleagues [63], was constructed. In our model, the incident $\lambda = 1064$ nm wavelength laser pulse was approximated with a flat-top spatial intensity profile and Gaussian temporal characteristics, with an intensity of $I = 7.5 \bullet 10^8$ W/cm$^2$ and a pulse length of $\tau = 8$ ns (FWHM). The absorption of light is described by the Beer–Lambert law, and the ablation mechanism was considered to be entirely photothermal ablation. In this case, the incident pulse is absorbed by the free electrons, which then transfer the energy to the entire lattice. The energy transfer takes place on the ps timescale, which is much shorter than the ns pulse duration, therefore, the ns pulse can be considered as a heat source. Since the temperature of the material rises well before the end of the incident pulse, the optical properties of the material must be considered with temperature-dependent parameters. Therefore, the reflection, absorption, and emission coefficients were derived from the

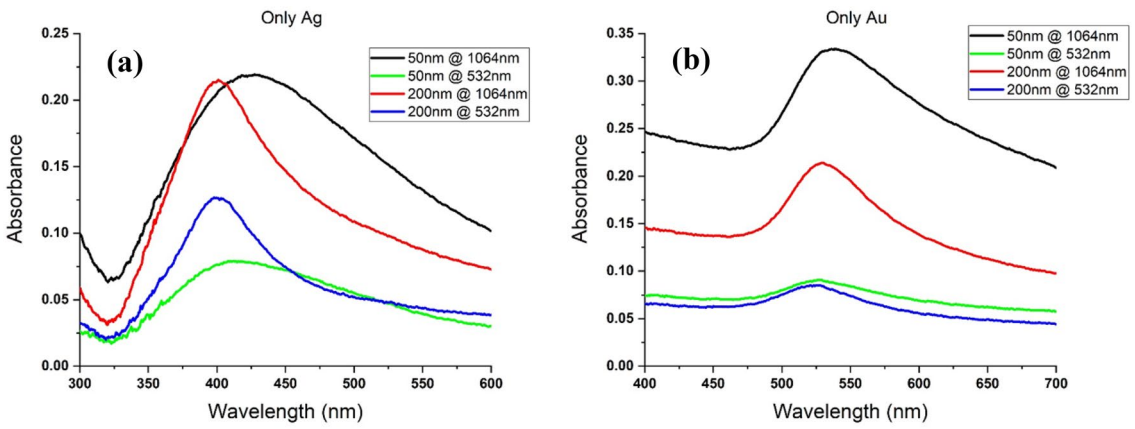


**Fig. 8** Absolute absorbance spectra of NP colloids produced by ablation of pure Ag (**a**) and pure Au (**b**) films using 1064 nm and 532 nm laser pulses

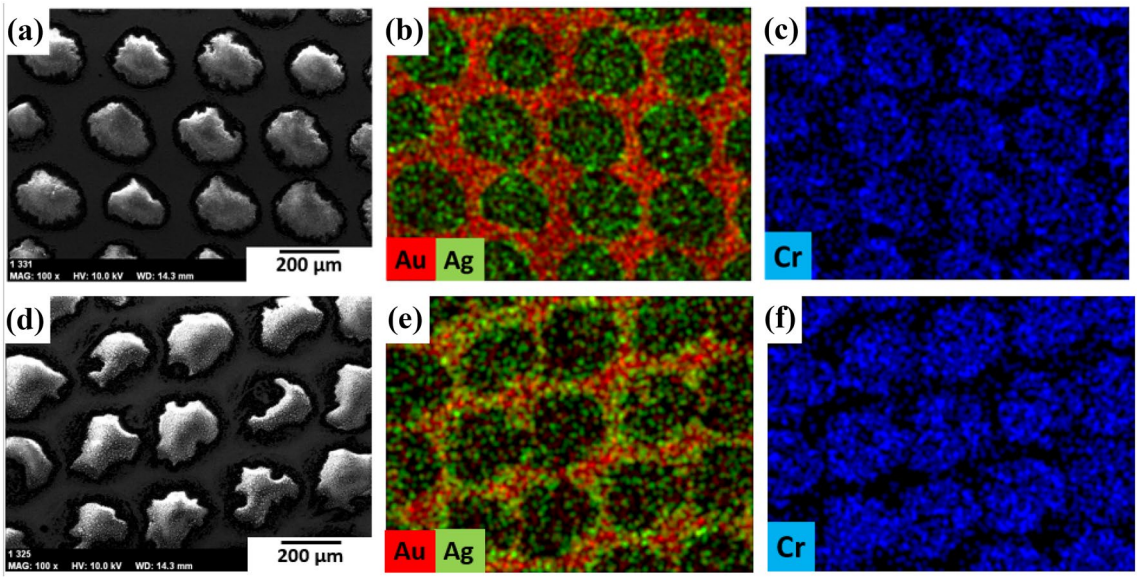


**Fig. 9** SEM images and EDX mappings (**a**–**c**: 200 nm Au–100 nm Ag, **d**–**f**: 50 nm Au–100 nm Ag) of the residual ablation craters

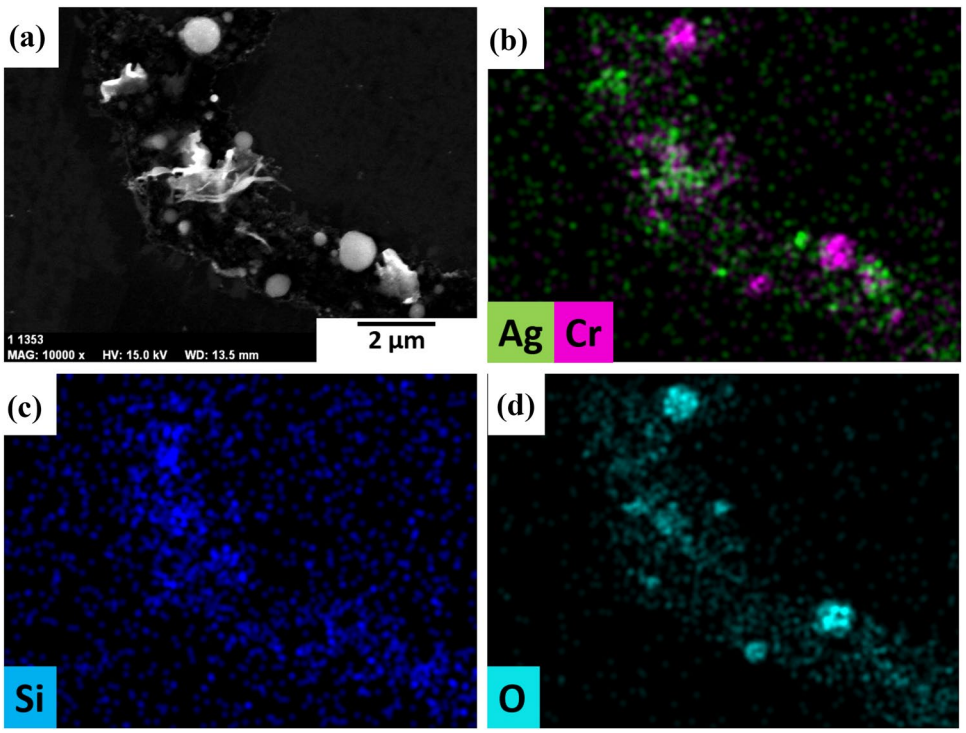


**Fig. 10** SEM image (**a**) and EDX element mappings (**b**–**d**) of a dried droplet of NP-colloid produced by PLAL. The substrate was 50 nm Ag film on fused silica and the colloid solution was dropped and dried on the surface of HOPG prior to analysis

complex refractive indices calculated from the Drude model. The dielectric function describing the light-matter interaction is given by $\varepsilon(\omega) = \varepsilon_1(\omega) - \varepsilon_2(\omega)$, in which, according to the Drude model,

$$\varepsilon_1(\omega) = 1 - \frac{\sigma_0 \tau}{\varepsilon_0} \frac{1}{\left[1 + (\omega\tau)^2\right]} \tag{1}$$

and

$$\varepsilon_2(\omega) = \frac{\sigma_0}{\varepsilon_0 \omega \left[1 + (\omega\tau)^2\right]}, \tag{2}$$

where $\tau = \frac{\sigma_0 m^*}{n_e e^2}$ is the collision time of electrons, $\sigma_0$ is the dc conductivity, $n_e = N_{val}\frac{\rho}{u}$ is the electron density, $N_{val}$ is the number of electrons in the valence band, $\rho$ and $u$ are the

density and molar weight of the matter, $\omega$ is the frequency of light, and $m^*$ is the effective electron mass. Out of these, $\sigma_0$ and $\rho$ are temperature-dependent, and $m^*$ is state-of-matter dependent parameters. Using these parameters and the $n = Re(\sqrt{\varepsilon})$, $k = Im(\sqrt{\varepsilon})$ relations, temperature-dependent complex refractive indices can be calculated, and from these, the temperature dependence of the optical coefficients are obtained (Fig. 11), using the relations $R = \left|\frac{n_{víz} - n_{arany}}{n_{víz} + n_{arany}}\right|^2$, $\alpha = \frac{4\pi k}{\lambda}$ and $\varepsilon = \frac{4n}{(n+1)^2 + k^2}$. In the absence of data, the relationships are extrapolated to extreme high temperatures.

For thermal ablation, the laser pulse as a heat source is described by

$$G(z,t) = I(t)(1-R)\frac{e^{\frac{-z}{\delta a}}}{\delta a}, \tag{3}$$

where $I(t)$ is the intensity of the pulse at a given moment, $R$ is the reflectivity and $\delta a$ is the penetration depth. The energy flow is governed by heat conduction, described as

$$\rho C_p \frac{\partial}{\partial} - \nabla(k\nabla T) = G(z,t), \tag{4}$$

where $\rho$ is the density, $C_p$ is the specific heat capacity, $T$ is the temperature, and $k$ is the thermal conductivity coefficient of the matter. Our model also takes into account the heat radiated and dissipated into the water environment with the equation $\vec{n}(k\nabla T) = q_0 + h\left(T_{water} - T\right) + \sigma\varepsilon\left(T^4_{water} - T^4\right)$.

The resulting temperature–time plots for 20 nm Au–100 nm Ag and 200 nm Au–100 nm Ag layer thickness combinations are shown in Fig. 12. The time profile of the incident laser pulse is also plotted in Fig. 12a. The graphs show that from the moment the laser pulse hits the surface, the surface temperature starts to increase rapidly. At around 3.2–4.5 ns, depending on the layer thickness, a short plateau in the temperature increase is visible, indicating the melting of the material. After melting is complete, the temperature rises rapidly again until the beginning of the evaporation (4.0–4.8 ns), where another plateau, slightly longer than the previous one, is visible. After the evaporation process, the surface temperature (not taking into account the mass ejection) rises again dramatically, peaking a few ns after the maximum of the incident pulse, at ~ 16 000 K. Thereafter, the temperature of the material starts to decrease. Comparing these results with the literature, we found that the evolution of the surface temperature is in good agreement with the previous calculations [64].

Figure 13 illustrates how the temperature changes in the irradiated volume element (inner circle) and its close surroundings during evaporation. Comparing the different layer thickness combinations, it can be seen in Fig. 13 (for the two most different thicknesses) that the thicker the gold layer, the later the temperature of the deeper regions will rise (both in the gold and the silver films), and the lower the peak temperature of these deeper regions will be. It is important to note that while at 20, 50, and 100 nm gold layer thicknesses the evaporation of the gold and silver films occurs quasi simultaneously, at 200 nm gold layer thickness this temporal overlap is very small (enlarged figures). A fundamental condition for the formation of composite NPs is the simultaneous presence of both elements in the plasma plume. This is fulfilled if evaporation occurs simultaneously from both layers. However, at 200 nm gold layer thickness gold is evaporated earlier than silver, and so alloying cannot happen. Consequently, our simulation result confirms our experimental observation that at a gold layer thickness of 200 nm, pure gold NPs are formed predominantly.

## 5 Conclusions

We have shown that Au–Ag composite NPs can be produced by PLAL of gold–silver multilayer targets and that the composition of the NPs can be varied by changing the absolute and relative thicknesses of the gold and silver layers.

SEM–EDX studies confirmed the spherical shape and the Au and Ag content of the NPs. However, since the exact Au:Ag ratio in the NPs remained unclear, we recorded the UV–VIS absorbance spectra of the NP colloids. We

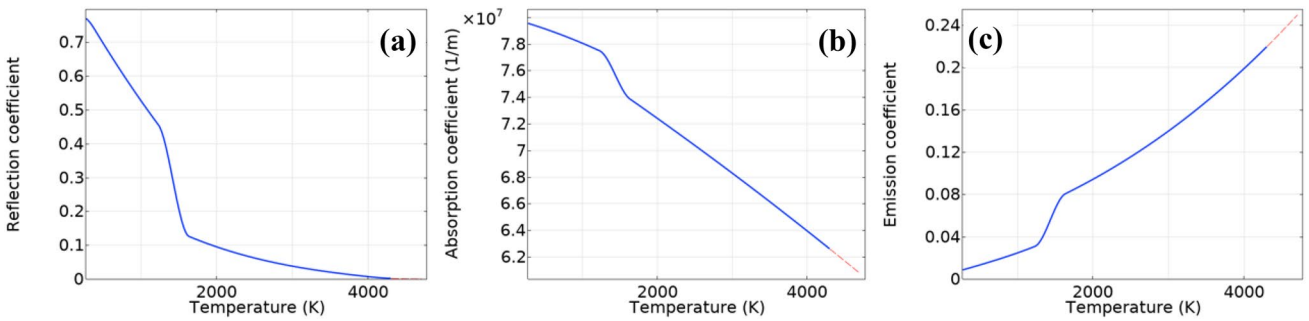


**Fig. 11** Temperature dependence of the reflection (**a**), absorption (**b**) and emission (**c**) coefficients, according to the Drude model

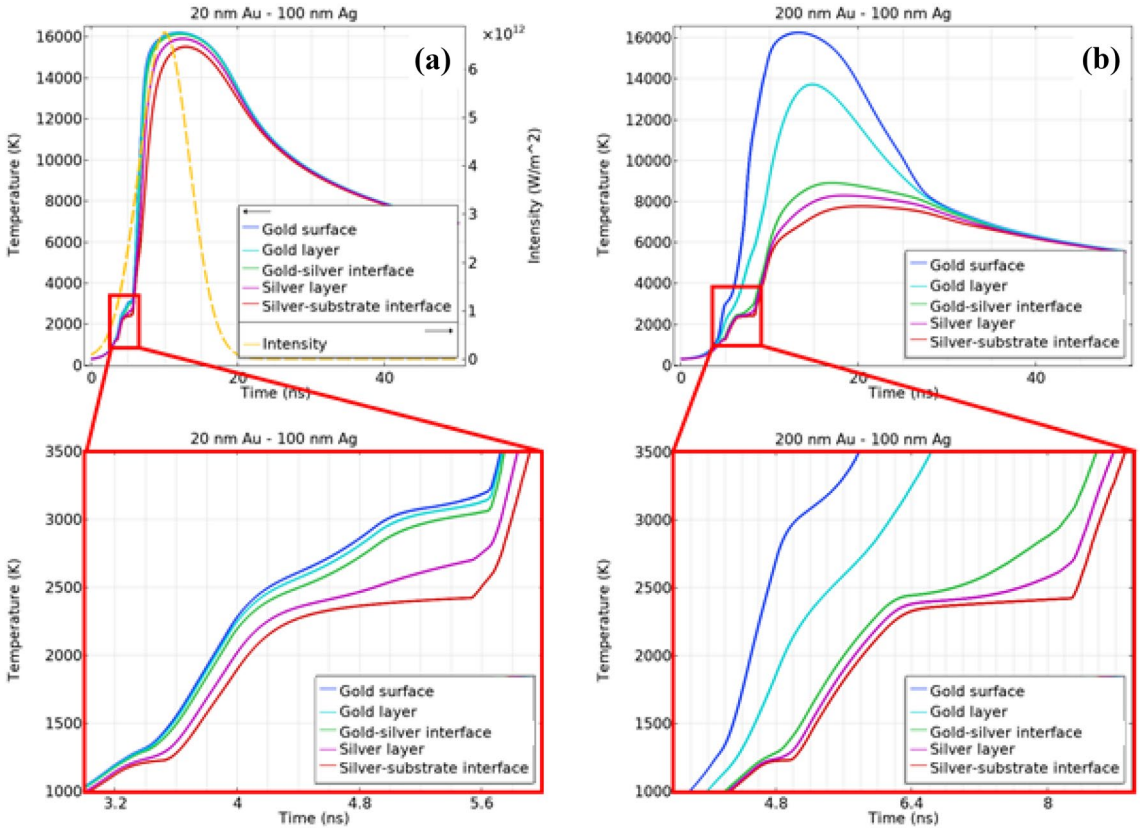


**Fig. 12** Time evolution of temperature in the layers and at layer interfaces; zoomed out images show the melting and evaporation range

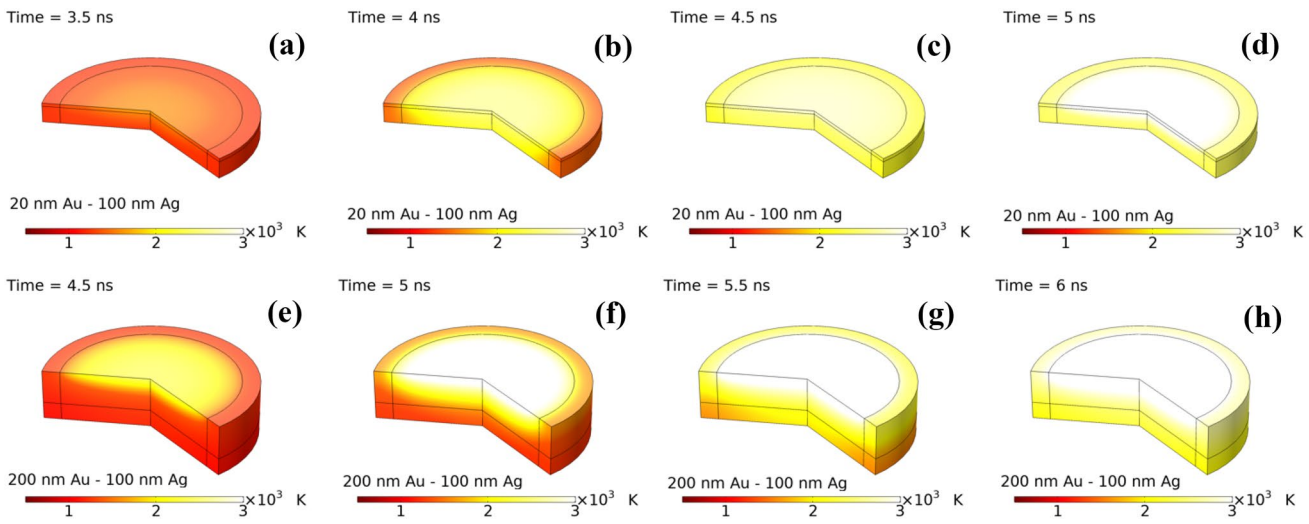


**Fig. 13.** 3D visualization of the temperature change in time in the evaporation regime. For illustrative purposes, the ratio of vertical to horizontal dimensions does not correspond to the actual, but the ratio of Au and Ag layer thicknesses does

investigated the position of the SPR peak in the spectra as a function of the relative thicknesses of the Au and Ag layers on the substrate. By comparing our observations with two theoretical models (Mie and BEM), we found that the position of the SPR peaks for different relative layer thicknesses is consistent with the SPR peak positions calculated for NPs with known Au:Ag compositions. This allowed us to demonstrate a direct correlation between the thickness and

composition of the Au–Ag layers on the substrate and the *average* composition of the NPs produced by PLAL.

However, for larger absolute layer thicknesses, the obtained NPs had a slightly different composition than expected based on the layer composition. To explain this, we developed a model to describe the ablation process for a layered target.

Assuming thermal ablation, our model showed that if one of the metals to be alloyed (in our case Ag) is too deep ($\geq 200$ nm) under the other metal layer (in our case Au layer), it is evaporated from the surface with a time delay, and thus the alloying is inherently impossible. Therefore, if the aim is to produce alloy NPs, it must be taken into account that there is a maximum thickness of the top layer up to which both layers can be ablated simultaneously.

We note that the total thickness of the multilayer cannot be arbitrarily thin either if we want to avoid ablation of the substrate material.

The advantage of NP production with PLAL of layered targets is that, despite its relatively low yield, it is a simple, clean and well-controlled technology. Considering that it applies widely implemented thin film technologies and well-established laser ablation in liquid procedures, it has great potential to produce nanomaterials with a complex structure and multiple functionalities of interest for cutting-edge applications in nanomedicine, catalysis, photonics and information technology. We assume that by varying the composition and the number/thickness of the layers, PLAL could be a straightforward method to create NPs that cannot be synthetized on other (e.g., chemical) ways.

**Acknowledgements** The financial support received from various sources including the Ministry of Innovation and Technology (through projects No. TUDFO/47138-1/2019-ITM FIKP and TKP2021-NVA-19) and the National Research, Development and Innovation Office (OTKA-K-138339) of Hungary are kindly acknowledged. The samples of the experiments were prepared using the infrastructure of ELI-ALPS Research Institute.

**Data availability** The data that support the findings of this study are available upon reasonable request from the authors.

## References

1. S.A.A. Rizvi, A.M. Saleh, Applications of nanoparticle systems in drug delivery technology. Saudi Pharm. J.: SPJ **26**, 64 (2018)
2. T. Gera, T. Smausz Kolumbán, T. Ajtai, B. Kurilla, Z. Homik, J. Kopniczky, Z. Bozoki, P. Szabó-Révész, R. Ambrus, B. Hopp, Production of ibuprofen-magnetite nanocomposites by pulsed laser ablation. J. Physics D: Applied Physics. **54**(39), 395401 (2021)
3. V. Amendola, M. Meneghetti, S. Fiameni, S. Polizzi, G. Fracasso, A. Boscaini, M. Colombatti, SERS labels for quantitative assays: Application to the quantification of gold nanoparticles uptaken by macrophage cells. Anal. Methods **3**, 849–856 (2011)
4. K.P. Tamarov, L.A. Osminkina, S.V. Zinovyev, K.A. Maximova, J.V. Kargina, Radio frequency radiation-induced hyperthermia using Si nanoparticle-based sensitizers for mild cancer therapy. Sci. Rep (2014). https://doi.org/10.1038/srep07034
5. C. Chen, G. Xing, J. Wang, Y. Zhao, B. Li, J. Tang, G. Jia, T. Wang, J. Sun, L. Xing, H. Yuan, Y. Gao, H. Meng, Z. Chen, F. Zhao, Z. Chai, X. Fang, Multihydroxylated [Gd@C82(OH)22] n nanoparticles: Antineoplastic activity of high efficiency and low toxicity. Nano Lett. **5**, 2050–2057 (2005)
6. E. Kymakis, G.D. Spyropoulos, R. Fernandes, G. Kakavelakis, A.G. Kanaras, E. Stratakis, Plasmonic bulk heterojunction solar cells: the role of nanoparticle ligand coating. ACS Photonics **2**, 714–723 (2015)
7. Y. Tong, H. Lee, W. Kang, H. Cho, Energy and exergy comparison of a flat-plate solar collector using water, Al2O3 nanofluid, and CuO nanofluid. Appl. Therm. Eng. **159**, 113959 (2019)
8. V. Lushta, D. Dietzel, B. Roling, A. Schirmeisen, Nanoscale characterization of ion mobility by temperature-controlled Li-nanoparticle growth. ACS Appl. Mater. Interfaces. **11**, 5476–5483 (2019)
9. V. Avasare, Z. Zhang, D. Avasare, I. Khan, A. Qurashi, Room-temperature synthesis of TiO2 nanospheres and their solar driven photoelectrochemical hydrogen production. Int J Energy Res. **39**, 1714–1719 (2015)
10. F. Ning, M. Shao, S. Xu, Y. Fu, R. Zhang, M. Wei, D.G. Evans, X. Duan, TiO 2 /graphene/NiFe-layered double hydroxide nanorod array photoanodes for efficient photoelectrochemical water splitting †. Energy Environ Sci **9**, 2633 (2016)
11. E.H. Lee, S.K. Lee, M.J. Kim, S.W. Lee, Simple and rapid detection of bisphenol A using a gold nanoparticle-based colorimetric aptasensor. Food Chem. **287**, 205–213 (2019)
12. T. Lee, S.Y. Park, H. Jang, G.H. Kim, Y. Lee, C. Park, M. Mohammadniaei, M.H. Lee, J. Min, Fabrication of electrochemical biosensor consisted of multi-functional DNA structure/porous au nanoparticle for avian influenza virus (H5N1) in chicken serum. Mater Sci Eng: C **99**, 511–519 (2019)
13. S. Unser, I. Bruzas, J. He, L. Sagle, Localized surface plasmon resonance biosensing: current challenges and approaches. Sensors. **15**, 15684–15716 (2015)
14. N. Tuccitto, L. Riela, A. Zammataro, L. Spitaleri, G. Li-Destri, G. Sfuncia, G. Nicotra, A. Pappalardo, G. Capizzi, G.T. Sfrazzetto, Functionalized carbon nanoparticle-based sensors for chemical warfare agents. ACS Applied Nano Materials **3**, 8182–8191 (2020)
15. A. Kohut, A. Kéri, V. Horváth, J. Kopniczky, T. Ajtai, B. Hopp, G. Galbács, Z. Geretovszky, Facile and versatile substrate fabrication for surface enhanced Raman spectroscopy using spark discharge generation of Au/Ag nanoparticles. Appl Surface Sci. **531**, 147268 (2020)
16. P. Liu, H. Chen, H. Wang, J. Yan, Z. Lin, G. Yang, Fabrication of Si/Au core/shell nanoplasmonic structures with ultrasensitive surface-enhanced raman scattering for monolayer molecule detection. J. Phys. Chem. C **119**, 1234–1246 (2015)
17. E. Giorgetti, P. Marsili, F. Giammanco, S. Trigari, C. Gellini, M. Muniz-Miranda, Ag nanoparticles obtained by pulsed laser ablation in water: surface properties and SERS activity. J. Raman Spectrosc. **46**, 462–469 (2015)
18. F. Tantussi, G.C. Messina, R. Capozza, M. Dipalo, L. Lovato, F. de Angelis, Long-range capture and delivery of water-dispersed nano-objects by microbubbles generated on 3d plasmonic surfaces. ACS Nano **12**(5), 4116–4122 (2018)
19. G. Marzun, A. Levish, V. Mackert, T. Kallio, S. Barcikowski, P. Wagener, Laser synthesis, structure and chemical properties of colloidal nickel-molybdenum nanoparticles for the substitution of noble metals in heterogeneous catalysis. J Colloid Interface Sci **489**, 57–67 (2017)

20. K.-H. Huynh, X.-H. Pham, J. Kim, S.H. Lee, H. Chang, W.-Y. Rho, B.-H. Jun, Synthesis, properties, and biological applications of metallic alloy nanoparticles. Int J Mol Sci. **21**, 5174 (2020)
21. C. Burda, X. Chen, R. Narayanan, M.A. El-Sayed, Chemistry and properties of nanocrystals of different shapes. Chem Rev. **105**(4), 1025–1102 (2005)
22. B. Li, S.H. Chan, PtFeNi tri-metallic alloy nanoparticles as electrocatalyst for oxygen reduction reaction in proton exchange membrane fuel cells with ultra-low Pt loading. Int. J. Hydrogen Energy **38**, 3338–3345 (2013)
23. G. Sharma, A. Kumar, S. Sharma, M. Naushad, R. Prakash Dwivedi, Novel development of nanoparticles to bimetallic nanoparticles and their composites: a review. J King Saud Univ-Sci **31**, 257–269 (2019)
24. Y.X. Gan, A.H. Jayatissa, Z. Yu, X. Chen, M. Li, Hydrothermal synthesis of nanomaterials. J Nanomater (2020). https://doi.org/10.1155/2020/8917013
25. P.-C. Chen, J.S. Du, B. Meckes, L. Huang, Z. Xie, J.L. Hedrick, V.P. Dravid, C.A. Mirkin, Structural evolution of three-component nanoparticles in polymer nanoreactors. J. Am. Chem. Soc. **139**, 9876–9884 (2017)
26. D. Amram, E. Rabkin, Core(Fe)–shell(Au) nanoparticles obtained from thin Fe/Au bilayers employing surface segregation. ACS Nano **8**, 10687–10693 (2014)
27. H.-C. Wu, C.-S. Chen, C.-M. Yang, M.-C. Tsai, J.-F. Lee, Decomposition of large Cu crystals into ultrasmall particles using chemical vapor deposition and their application in selective propylene oxidation. ACS Appl. Mater. Interfaces. **10**, 38547–38557 (2018)
28. L.Q. Long, T.T.B. Hue, N.X. Hoan, L.V. Cuong, P.D. Thang, T. Hoang, T.A. Truc, Growth mechanism and stability of magnetite nanoparticles synthesized by the hydrothermal method. J. Nanosci. Nanotechnol. **16**, 7373–7379 (2016)
29. G. Gahlawat, A.R. Choudhury, A review on the biosynthesis of metal and metal salt nanoparticles by microbes. RSC Adv. **9**, 12944–12967 (2019)
30. P. Singh, Y.J. Kim, D. Zhang, D.C. Yang, Biological synthesis of nanoparticles from plants and microorganisms. Trends Biotechnol. **34**, 588–599 (2016)
31. D. Sharma, S. Kanchi, K. Bisetty, Biogenic synthesis of nanoparticles: a review. Arab. J. Chem. **12**, 3576–3600 (2019)
32. B. Malik, T.B. Pirzadah, M. Kumar, R.U. Rehman, Biosynthesis of nanoparticles and their application in pharmaceutical industry. Nanotechnol Food Environmental Paradigm **235**, 52 (2017)
33. T.A. Simoes, A.E. Goode, A.E. Porter, M.P. Ryan, S.J. Milne, A.P. Brown, R.M.D. Brydson, Microstructural characterization of low and high carbon CoCrMo alloy nanoparticles produced by mechanical milling. J. Phys: Conf. Ser. **522**, 012059 (2014)
34. N. Naseri, P. Sangpour, S.H. Mousavi, Applying alloyed metal nanoparticles to enhance solar assisted water splitting. RSC Adv. **4**, 46697–46703 (2014)
35. M. Wagner, A. Kohut, Z. Geretovszky, M. Seipenbusch, G. Galbács, Observation of fine-ordered patterns on electrode surfaces subjected to extensive erosion in a spark discharge. J. Aerosol Sci. **93**, 16–20 (2016)
36. L. Égerházi, B. Kovács, T. Szörényi, Spectroscopic quantification of the nanoparticle production efficiency of copper wire explosion. J. Appl. Phys. **129**, 195902 (2021)
37. V. Amendola, M. Meneghetti, Laser ablation synthesis in solution and size manipulation of noble metal nanoparticles. Phys. Chem. Chem. Phys. **11**, 3805–3821 (2009)
38. J. Xiao, P. Liu, C.X. Wang, G.W. Yang, External field-assisted laser ablation in liquid: An efficient strategy for nanocrystal synthesis and nanostructure assembly. Prog. Mater Sci. **87**, 140–220 (2017)
39. H. Zeng, X.-W. Du, S.C. Singh, S.A. Kulinich, S. Yang, J. He, W. Cai, Nanomaterials via Laser Ablation/Irradiation in Liquid: A Review. Adv. Func. Mater. **22**, 1333–1353 (2012)
40. V. Amendola, M. Meneghetti, What controls the composition and the structure of nanomaterials generated by laser ablation in liquid solution? Phys. Chem. Chem. Phys. **15**, 3027–3046 (2013)
41. S. Dittrich, S. Barcikowski, B. Gökce, S. Dittrich, S. Barcikowski, B. Gökce, Plasma and nanoparticle shielding during pulsed laser ablation in liquids cause ablation efficiency decrease. Opto-Electronic Advances **4**, 200072–200081 (2021)
42. D. Zhang, B. Gökce, S. Barcikowski, Laser synthesis and processing of colloids: fundamentals and applications. Chem. Rev. **117**, 3990–4103 (2017)
43. D. Zhang, Z. Li, K. Sugioka, Laser ablation in liquids for nanomaterial synthesis: diversities of targets and liquids. J Physics: Photonics **3**, 042002 (2021)
44. A. Kanitz, M.R. Kalus, E.L. Gurevich, A. Ostendorf, S. Barcikowski, D. Amans, Review on experimental and theoretical investigations of the early stage, femtoseconds to microseconds processes during laser ablation in liquid-phase for the synthesis of colloidal nanoparticles. Plasma Sources Sci Technol. **28**, 103001 (2019)
45. I. Lee, S.W. Han, K. Kim, Production of Au–Ag alloy nanoparticles by laser ablation of bulk alloys. Chem. Commun. **1**, 1782–1783 (2001)
46. A. Neumeister, J. Jakobi, C. Rehbock, J. Moysig, S. Barcikowski, Monophasic ligand-free alloy nanoparticle synthesis determinants during pulsed laser ablation of bulk alloy and consolidated microparticles in water. Phys. Chem. Chem. Phys. **16**, 23671–23678 (2014)
47. A. Tymoczko, M. Kamp, C. Rehbock, L. Kienle, E. Cattaruzza, S. Barcikowski, V. Amendola, One-step synthesis of Fe–Au core–shell magnetic-plasmonic nanoparticles driven by interface energy minimization. Nanoscale Horizons **4**, 1326–1332 (2019)
48. R.G. Nikov, N.N. Nedyalkov, P.A. Atanasov, D.B. Karashanova, Synthesis of bimetallic nanostructures by nanosecond laser ablation of multicomponent thin films in water. J. Phys: Conf. Ser. **992**, 012046 (2018)
49. A.A. Nastulyavichus, S.I. Kudryashov, N.A. Smirnov, A.A. Rudenko, A.Y. Kharin, N.I. Busleev, D.A. Zayarny, A.A. Ionin, D.A. Kirilenko, P.N. Brunkov, Novel approach of controllable stoichiometric fabrication of alloyed Au/Ag nanoparticles by nanosecond laser ablation of thin bi-layered films in water. Laser Phys. Lett. **16**, 096002 (2019)
50. Nikov R G, Nedyalkov N N, Nikolov A S, Atanasov P A, Alexandrov M T and Karashanova D B 2015 Formation of bimetallic nanoparticles by pulsed laser ablation of multicomponent thin films in water 151–7. https://doi.org/10.1117/12.2175638 9447
51. R.G. Nikov, N.N. Nedyalkov, R.G. Nikov, D.B. Karashanova, Nanosecond laser ablation of Ag–Au films in water for fabrication of nanostructures with tunable optical properties. Appl Phys A: Mater Scie Process. **124**, 1–9 (2018)
52. V. Amendola, S. Scaramuzza, F. Carraro, E. Cattaruzza, Formation of alloy nanoparticles by laser ablation of Au/Fe multilayer films in liquid environment. J. Colloid Interface Sci. **489**, 18–27 (2017)
53. Z. Lin, J. Yue, L. Liang, B. Tang, B. Liu, L. Ren, Y. Li, L. Jiang, Rapid synthesis of metallic and alloy micro/nanoparticles by laser ablation towards water. Applied Surface Sci. **504**, 144461 (2020)
54. C.Y. Shih, C. Chen, C. Rehbock, A. Tymoczko, U. Wiedwald, M. Kamp, U. Schuermann, L. Kienle, S. Barcikowski, L. Zhigilei, v., Limited elemental mixing in Nanoparticles Generated By ultrashort pulse laser ablation of AgCu bilayer thin films in a liquid environment: atomistic modeling and experiments. J Phys Chem C. **125**(3), 2132–2155 (2021)
55. Anon MiePlot

56. U. Hohenester, A. Trügler, MNPBEM–A Matlab toolbox for the simulation of plasmonic nanoparticles. Computer Phys Commun. **183**, 370–381 (2012)
57. D. Rioux, S. Vallières, S. Besner, P. Muñoz, E. Mazur, M. Meunier, An analytic model for the dielectric function of Au Ag, and their Alloys. Advanced Optical Materials **2**, 176–182 (2014)
58. M. Brückner, J.H. Schäfer, C. Schiffer, J. Uhlenbusch, Measurements of the optical constants of solid and molten gold and tin at λ=10.6. J Appl Phys. **70**, 1642 (1998)
59. L.N. Aksyutov, Normal spectral emissivity of gold, platinum, and tungsten. J Eng phys. **27**(2), 913–917 (1974)
60. M.F. Becker, J.R. Brock, H. Cai, D.E. Henneke, J.W. Keto, J. Lee, W.T. Nichols, H.D. Glicksman, Metal nanoparticles generated by laser ablation. Nanostruct. Mater. **10**, 853–863 (1998)
61. T. Bai, P. Lu, K. Zhang, P. Zhou, Y. Liu, Z. Guo, X. Lu, Gold/silver bimetallic nanocrystals: Controllable synthesis and biomedical applications. J. Biomed. Nanotechnol. **13**, 1178–1209 (2017)
62. I. Isnaeni, Y. Herbani, Aggregation effect on absorbance spectrum of laser ablated gold nanoparticles. J Phys: Conf Series. **817**, 012039 (2017)
63. X. Chen, Y. Chen, M. Yan, M. Qiu, Nanosecond photothermal effects in plasmonic nanostructures. ACS Nano **6**, 2550–2557 (2012)
64. Anon (PDF) Laser-induced plasma as a function of the laser parameters and the ambient gas